

# Detailed single crystal EPR lineshape measurements for the single molecule magnets $\text{Fe}_8\text{Br}$ and $\text{Mn}_{12}-\text{ac}$

S. Hill<sup>†</sup>

*Department of Physics, University of Florida, Gainesville, FL 32611*

S. Maccagnano

*Department of Physics, Montana State University, Bozeman, MT 59717*

Kyungwha Park

*School of Computational Science and Information Technology and Department of Chemistry,*

*Florida State University, Tallahassee, FL 32606*

R. M. Achey, J. M. North and N. S. Dalal

*Department of Chemistry and National High Magnetic Field Laboratory, Florida State*

*University, Tallahassee, FL 32306*

(December 2, 2024)

It is shown that our multi-high-frequency (40 – 200 GHz) resonant cavity technique yields distortion-free high field EPR spectra for single crystal samples of the uniaxial and biaxial spin  $S = 10$  single molecule magnets (SMMs)  $[\text{Mn}_{12}\text{O}_{12}(\text{CH}_3\text{COO})_{16}(\text{H}_2\text{O})_4]\cdot 2\text{CH}_3\text{COOH}\cdot 4\text{H}_2\text{O}$  and  $[\text{Fe}_8\text{O}_2(\text{OH})_{12}(\text{tacn})_6]\text{Br}_8 \cdot 9\text{H}_2\text{O}$ . The observed lineshapes exhibit a pronounced dependence on temperature, magnetic field, and the spin quantum numbers ( $M_S$  values) associated with the levels involved in the transitions. Measurements at many frequencies allow us to separate various contributions to the EPR linewidths, including significant  $D$ -strain,  $g$ -strain and broadening due to the random dipolar fields of neighboring molecules. We also identify asymmetry in some of the EPR lineshapes for  $\text{Fe}_8$ , and a previously unobserved fine structure to some of the EPR lines for both the  $\text{Fe}_8$  and  $\text{Mn}_{12}$  systems. These findings prove relevant to the mechanism of quantum tunneling of magnetization in these SMMs.

PACS numbers: 76.30.-v, 75.50.Xx, 75.45.+j

## I. Introduction

Examples of "single molecule magnets" (SMMs) which have attracted considerable recent interest include the uniaxial  $[\text{Mn}_{12}\text{O}_{12}(\text{CH}_3\text{COO})_{16}(\text{H}_2\text{O})_4] \cdot 2\text{CH}_3\text{COOH} \cdot 4\text{H}_2\text{O}$  ( $\text{Mn}_{12}$ –acetate, or  $\text{Mn}_{12}$ –ac) system, and the biaxial  $[\text{Fe}_8\text{O}_2(\text{OH})_{12}(\text{tacn})_6]\text{Br}_8 \cdot 9\text{H}_2\text{O}$  ( $\text{Fe}_8\text{Br}$ ) system [1,2,3,4,5,6,7,8,9,10]. Both of these SMMs exhibit spin  $S = 10$  ground states, with a dominant easy-axis type anisotropy,  $D\hat{S}_z^2$  (where  $D$  is negative – see section II), which provides a potential barrier (height  $\sim |D|S^2$ ) against the reversal of individual spins from  $M_S = +10$  to  $-10$  (see Fig. 1). Recent studies have shown that both systems possess an ability for their magnetic moments to quantum tunnel through their respective anisotropy barriers (see Fig. 1), and that this process dominates the magnetization dynamics at low temperatures ( $k_B\text{T} \ll |D|S^2$ ) [5,11,12,13,14,15,16,17,18].

Because of its significance as a fundamentally novel phenomenon, as well as its potential for applications in nano-technology, magnetic quantum tunneling (MQT) in SMMs has been extensively studied lately (see *e.g.* [5,11,12,13,14,15,16,17,18]), yet its underlying mechanism is still not fully understood, especially at a quantitative level. One possible reason is the lack of precise information on the disposition of the individual (electronic) spin energy levels. This is due to the fact that much of the available data on the spin properties of these systems have been obtained through DC and AC magnetization studies [14,15,16,19], specific heat [20], neutron scattering [21,22,23], proton NMR [24,25], and muon spin relaxation [24], which cannot easily or directly probe the properties of specific spin quantum levels.

An important breakthrough in the spectroscopy of SMMs has been the development of a sensitive cavity perturbation technique for carrying out multi-high-frequency (40 to  $> 200$  GHz) EPR measurements on single crystals [26,27,28,29,30]. In particular, this technique leads to at least a three orders of magnitude improvement in detection sensitivity [28] relative to conventional single-pass multi-high-frequency EPR techniques [8,31,32,33,34,35,36], which opens up many new avenues for probing SMMs. To date, our single crystal investigations have focused primarily on the energy dependence of the positions in magnetic field of EPR

absorptions corresponding to transitions between different spin quantum levels [26,27,28,29]. In this article, we turn our attention to the magnetic field, frequency, temperature and spin quantum level ( $M_S$ ) dependence of the EPR linewidths and, in particular, the line shapes obtained from measurements on  $\text{Fe}_8\text{Br}$  and  $\text{Mn}_{12}-\text{ac}$ . We note that a brief account has been presented earlier [37]. However, this earlier report emphasizes the theoretical foundations of the linewidth analysis, and does not consider lineshapes.

Essentially all previous high frequency EPR investigations of  $\text{Fe}_8\text{Br}$  and  $\text{Mn}_{12}-\text{ac}$  suffer from either a lack of resolution, sensitivity and/or experimental artifacts. It is commonly stated that observed EPR lineshapes cannot be analyzed because they usually contain uncontrollable distortions due to instrumental artifacts resulting from standing waves in the sample probe, which cause a mixing of the dissipative and reactive sample response [32,33,38]. This is particularly true in the case of the high magnetic field studies of Barra *et al.* [8,32,33,34]; asymmetric lineshapes are generally observed, making it extremely difficult to evaluate the true resonance positions. Indeed, even for aligned polycrystals, significant discrepancies can be noted between the observed and calculated EPR transitions, with respect to both the peak positions and intensities, as well as the line shapes and widths [33]. As an example, it has been reported in [33] that the linewidths in  $\text{Fe}_8\text{Br}$  approximately scale as  $M_S^2$ , whereas our earlier studies [29,37] have shown a dominant linear dependence of the linewidths on  $M_S$ , both for  $\text{Fe}_8\text{Br}$  and  $\text{Mn}_{12}-\text{ac}$ . In view of this fact, and the strongly asymmetric lineshapes observed in high field EPR studies, one has to question the precision of the spin Hamiltonian parameters deduced by single-pass (*i.e.* cavity-less) high-field EPR. The zero field coherent time-domain THz technique employed by Parks *et al.* [36], suffers from a lack of resolution (at best, the energy resolution is a fifth of the broadest EPR line width), as well as sensitivity. Consequently, it is necessary to study a large sample made up from unaligned microcrystals; even then, it is only possible to observe a few transitions, and experimental complications only permit a linewidth analysis, *i.e.* no lineshape analysis is possible. To date, the most precise SMM EPR lineshape analyses have been reported by Mukhin *et al.*, for both  $\text{Fe}_8\text{Br}$  and  $\text{Mn}_{12}-\text{ac}$  [35], using a zero-field coherent source technique. Gaussian

EPR lines are observed, which are attributed to random dipolar fields in the sample. However, these studies also suffer from lack of sensitivity. Consequently, only a few transitions are observed, even for very large polycrystalline samples. Finally, conventional X-band EPR is limited by the fact that only a few transitions close to the top of the barrier are accessible. Furthermore, little or no information concerning the spin-spin ( $T_2$ ) and spin-lattice ( $T_1$ ) relaxation times has been possible in X-band [38].

As we will show in this article, measurements on single crystals are essential, as are several other unique aspects of our technique. For example, contrary to recent assertions by Blinc *et al.* [38], we are able to obviate essentially all instrumental artifacts that could influence/distort EPR line shapes. In addition, our ability to measure at many frequencies, temperatures and orientations enables us to distinguish between several contributions to the EPR line widths and shapes. These include: inter-SMM and hyperfine dipolar fields; distributions in crystal field parameters; and spin-lattice interactions. Indeed, each of these effects have been discussed in the literature in terms playing a possible role in the MQT phenomenon, *e.g.* dipolar fields [39], distributed crystal field parameters caused by dislocations [40], thermally assisted tunneling [14,41,42], the Landau-Zener effect [43,44,45], and hyperfine interactions [46,47]. Based on our recent theoretical work [37], we find that a distribution in the uniaxial crystal field parameter, so called  $D$ –strain, contributes significantly to the EPR linewidths for the  $\text{Fe}_8\text{Br}$  and  $\text{Mn}_{12} - ac$  systems. In addition, we observe an appreciable inter-SMM dipolar broadening for  $\text{Fe}_8\text{Br}$ , and  $g$ –strain in  $\text{Mn}_{12} - ac$ . The current work focuses on the EPR lineshapes. This is particularly important in view of recent theoretical work [40] which considers local distortions in the SMM site symmetries, and their role in the MQT phenomenon.

The article is organized as follows: in the next section (II), we discuss the  $S = 10$  effective spin Hamiltonian in the context of high-frequency EPR and the MQT phenomenon; in section III we describe our experimental procedure; in section IV, we separately present results for  $\text{Fe}_8\text{Br}$  (IV. A) and  $\text{Mn}_{12} - ac$  (IV. B); in section V, we discuss the significance of our results, and we summarize and conclude our findings in section VI.

## II. The effective spin Hamiltonian

The effective spin Hamiltonian for the  $\text{Mn}_{12} - ac$  and  $\text{Fe}_8\text{Br}$  systems has the form:

$$\hat{H} = D\hat{S}_z^2 + E(\hat{S}_x^2 - \hat{S}_y^2) + \mu_B \vec{B} \cdot \vec{g} \cdot \vec{S} + \hat{O}_4 + \hat{H}' ; \quad (1)$$

where  $\vec{S}$  is the vector spin operator and  $\hat{S}_z$ ,  $\hat{S}_x$  and  $\hat{S}_y$  are the spin projection operators along the easy, hard and intermediate axes respectively;  $D$  is the uniaxial spin-spin coupling parameter and the rhombic  $E$  ( $< D/3$ ) term characterizes the magnetic anisotropy in the plane perpendicular to the easy axis;  $\vec{g}$  is the Landé g-tensor and  $\vec{B}$  is the applied magnetic field vector; finally,  $\hat{O}_4$  denotes weaker higher order terms of order four in the spin operators, and  $\hat{H}'$  represents additional perturbations such as those which lead to EPR line broadening, as discussed in the introduction.  $D$  is negative for both  $\text{Mn}_{12} - ac$  ( $= -0.457 \text{ cm}^{-1}$  [22]) and  $\text{Fe}_8\text{Br}$  ( $= -0.203 \text{ cm}^{-1}$  [23]). The rhombic term  $E$  is zero for  $\text{Mn}_{12}-ac$ , due to its strictly axial ( $S_4$ ) site symmetry, while  $E = 0.032 \text{ cm}^{-1}$  for  $\text{Fe}_8\text{Br}$  [23]. For a cylindrically symmetric system, for which  $D\hat{S}_z^2$  would be the only non-zero term in Eq. (1) in zero applied field, the energy eigen states may be labeled by the quantum number  $M_S$  ( $-S < M_S < S$ ), which represents the projection of  $S$  onto the easy axis; the energy eigenvalues are then given by the expression  $\epsilon = DM_S^2$ . This results in the energy barrier separating doubly degenerate ( $M_S = \pm i$ ,  $i = \text{integer}$ ) spin "up" and "down" states (see Fig. 1).

In order for quantum tunneling to be possible, there must exist finite terms in Eq. (1) that break the cylindrical symmetry (*i.e.* do not commute with  $\hat{S}_z$ ) and mix states in either potential well, thereby lifting the  $M_S = \pm i$  degeneracies. Such terms include: the rhombic  $E(\hat{S}_x^2 - \hat{S}_y^2)$  term; higher order single-ion anisotropy terms in the transverse spin operators (*e.g.*  $\hat{S}_x^4$  and  $\hat{S}_y^4$ ) [8,16,22]; a transverse externally applied magnetic field; transverse internal fields due to neighboring SMMs or nuclei (contained in  $\hat{H}'$  [39,46]); or local distortions in the crystal field symmetry caused imperfections in the crystal (also contained in  $\hat{H}'$  [40]) – these may include dislocations, or a partial loss or disorder among the ligand molecules. Pure quantum tunneling is observed between the unperturbed  $M_S = \pm 10$

degenerate ground states in  $\text{Fe}_8\text{Br}$  below about 350 mK (see Fig. 1), and the observed relaxation has been explained in terms of the  $E(\hat{S}_x^2 - \hat{S}_y^2)$  term in Eq. (1) [48]. However, one has to additionally consider the respective roles of inter-SMM dipolar fields and nuclear hyperfine fields [ $\hat{H}'$  in Eq. (1)] in order to fully account for the observed tunneling in  $\text{Fe}_8\text{Br}$  [18,46]. For the  $\text{Mn}_{12}-\text{ac}$  system, the situation is even more complex: pure ground state quantum tunneling has not been observed, and there is little consensus as to the origin of the apparent (weak) transverse anisotropy which causes thermally assisted quantum tunneling among levels near the top of the barrier (see Fig. 1). The leading theories include: fourth order single ion transverse anisotropy terms such as  $\hat{S}_x^4 + \hat{S}_y^4$ , which are allowed under the axial ( $S_4$ ) site symmetry [8,16,22]; and local distortions in the axial crystal fields caused, *e.g.* by dislocations [40].

A tunneling matrix element (term in Eq. 1 that does not commute with  $\hat{S}_z$ ) gives rise to eigenstates that are constructed from symmetric and antisymmetric combinations of unperturbed ( $M_S = \pm i$ ) states on either side of the barrier, and to a lifting of the degeneracy (tunnel splitting) between these symmetric and antisymmetric states. Thus, the tunneling matrix elements modify the energy eigenvalues and should, therefore, be detectable in an EPR experiment. However, for the systems of interest, these effects are small. Consequently, great precision is required. Although inelastic neutron scattering (INS) measurements are capable of providing similar information, EPR offers many advantages in terms of resolution, sensitivity (amount of sample required) and, in particular, the fact that one can systematically control the level mixing by means of an externally applied magnetic field. In addition, the higher sensitivity of the EPR technique assures that all of this may be achieved for a single crystal. Several EPR (and INS) experiments have indicated the presence of significant fourth order single-ion transverse anisotropies for both  $\text{Mn}_{12} - \text{ac}$  [16,26,32,35] and  $\text{Fe}_8\text{Br}$  [33,35]. Nevertheless, fourth order anisotropy *cannot* fully explain the observed frequency of magnetization steps observed in low temperature hysteresis experiments [49], and there remains considerable disagreement as to the magnitude of the fourth order terms [16,26,32,33,34,35,51]. Consequently, higher resolution EPR measurements are necessary in

order to refine estimates of the Hamiltonian parameters, and to determine whether EPR lineshapes contain additional information concerning the MQT phenomenon.

### III. Experimental

The  $(2S + 1)$ -fold quantum energy level structure associated with a large molecular spin  $S$  necessitates spectroscopies spanning a wide frequency range. Furthermore, large zero-field level splittings, due to the significant crystalline anisotropy (large  $|D|$ ) and large spin, demand the use of frequencies and magnetic fields considerably higher (50 GHz to 1 THz, and up to 10 tesla respectively) than those typically used by the majority of EPR spectroscopists. The high degree of sensitivity required for single crystal measurements is achieved using a resonant cavity perturbation technique in combination with a broad-band Millimeter-wave Vector Network Analyzer (MVNA) exhibiting an exceptionally good signal-to-noise ratio; a detailed description of this instrumentation can be found in ref. [28,52]. The MVNA is a phase sensitive, fully sweepable (8 to 350 GHz [53]), superheterodyne source/detection system. Several sample probes couple the network analyzer to a range of high sensitivity cavities ( $Q$ -factors of up to 25,000) situated within the bore of a 7 tesla superconducting magnet. The MVNA/cavity combination has been shown to exhibit a sensitivity of at least  $10^9$  spins $\cdot$ G $^{-1}\cdot$ s $^{-1}$ , which is comparable with the best narrow-band EPR spectrometers. This, coupled with newly acquired sources and a split-pair magnet, allow single crystal measurements at any frequency in the range from 8 to 250 GHz, at temperatures down to 1.5 K ( $\pm 0.01$ K), and for any geometrical combination of DC and AC field orientations up to 7 T (up to 45 T at the National High Magnetic Field Laboratory).

The use of a narrow band cavity offers many important advantages over non-resonant methods (see *e.g.* refs [8,31,32,33,34]). Careful consideration concerning the coupling of radiation to and from the cavity (via waveguide), combined with the ability to study very small samples, eliminates problems associated with standing waves in the sample probe [52]. This, in turn, eliminates a mixing of the dissipative and reactive responses of the sample under investigation and, when combined with a vector detection scheme, enables

faithful extraction of the true EPR lineshapes (both the real and imaginary components), free from instrumental artifacts. One other notable feature of the superheterodyne scheme is its detection rate of 34 MHz; thus, there is no need for field modulation, unlike other high field EPR methods [8,31,32,33]. Consequently, any raw data displayed in this paper constitutes pure absorption. Finally, the use of a cavity enables positioning of a single crystal sample into a well defined electromagnetic field environment, *i.e.* the orientations of the DC and AC magnetic fields relative to the sample's crystallographic axes is precisely known, and the DC field is very homogeneous over the tiny volume ( $\ll 1\text{mm}^3$ ) of the sample. In this way, additional contributions to the EPR lineshapes are avoided due to, *e.g.* field inhomogeneities over the sample volume, or slight mis-alignments of crystallites, as may be the case for measurements on aligned powders.

Single  $\text{Mn}_{12}-\text{ac}$  and  $\text{Fe}_8\text{Br}$  crystals were grown using literature methods [2,7]. All measurements were performed in the standard EPR configuration with the AC excitation field transverse to the DC field. The  $\text{Fe}_8\text{Br}$  crystal used for the majority of the studies reported in the following section was a thin rhombic (acute angle  $\sim 60^\circ$ ) platelet with edges of length 0.7 mm, and thickness 0.17 mm. The  $\text{Mn}_{12}-\text{ac}$  crystal was needle shaped, with approximate dimensions  $1 \times 0.15 \times 0.05 \text{ mm}^3$ . Orientation of  $\text{Mn}_{12}-\text{ac}$  crystal was straightforward, due to the fact that its easy axis is defined by the needle axis of the sample. Alignment of the  $\text{Fe}_8\text{Br}$  crystal necessitated measurements at many angles [29]. All of the data presented in this paper were obtained with the DC magnetic field aligned approximately parallel to the samples' easy axes (hard axis data are presented elsewhere [26,29]). Finally, temperature control, in the range 2 to 50 K, was achieved using a variable flow cryostat situated within the bore of the superconducting magnet.

## IV. Results

### A. $\text{Fe}_8\text{Br}$

Figure 2 shows raw temperature dependent data obtained for the  $\text{Fe}_8\text{Br}$  SMM at a frequency of 116.931 GHz; the field is applied along the easy axis to within an accuracy of about  $1^\circ$ .

A series of more-or-less evenly spaced resonant absorptions are observed which become successively weaker with increasing field. A detailed analysis of the frequency dependence of the EPR line positions is published elsewhere [29]. Here we focus instead on the line widths and shapes. In this frequency and field range, and for this orientation, the levels involved in the transitions are well separated and do not cross. Thus,  $M_S$  is a good quantum number, and we have labeled the resonances in Fig. 2 according to the levels involved in the transitions.

It is apparent from Fig. 2 that the observed transitions exhibit dramatic variations in linewidth, both as a function of  $M_S$ , field and temperature. In order to characterize this width dependence, it is first necessary to fit the line shapes. Fig. 3 shows several attempts to fit various transitions with both Lorentzian and Gaussian functions; all of the data were obtained from a single field sweep at a frequency of 89.035 GHz and a temperature of 10 K, with the field close to alignment with the easy axis ( $8^\circ \pm 1^\circ$ ). At the lowest fields, where the resonances are broad (comparable to spacings) and therefore overlap, fits involving multiple Gaussian or Lorentzian functions are necessary (Fig. 3). As can be seen from this figure, the Gaussian fit is considerably better than the Lorentzian one, suggesting that some form of inhomogeneous broadening mechanism is at play. Although this has been noted by other authors [35], these earlier measurements were performed on polycrystalline powders, which were pressed into large pellets. Consequently, the microcrystals in the pellet will have been subjected to varying stresses that could be responsible for the broad Gaussian lines. Here, we demonstrate that this is an intrinsic feature of the  $\text{Fe}_8$  SMMs (this is also the case for  $\text{Mn}_{12}$  – see following section).

Fig. 4 shows Lorentzian and Gaussian fits to transitions excited from successively higher  $M_S$  levels (smaller absolute value of  $M_S$ ) from the same field sweep as the data in Fig. 3. The first thing to note is the dramatic line narrowing with decreasing absolute value of  $M_S$ . It is also apparent that, inspite of the reduced signal-to-noise, a crossover in lineshape from Gaussian to Lorentzian can clearly be established as the lines become narrower. The significance of this finding will be discussed further below.

Figure 5 shows a compilation of Gaussian widths, versus  $M_S$  (the level from which the transition was excited), measured at many different frequencies; all of the data were obtained at a temperature of 10 K, and with the field applied at an angle  $\theta = 8^\circ \pm 1^\circ$  away from the easy axis. The pronounced (almost linear) increase in EPR linewidth with  $M_S$  is due to  $D$ -strain [37]. Since the dominant contribution to the spin Hamiltonian (Eq. 1) is proportional to  $M_S^2$ , energy differences (*i.e.* EPR transition frequencies) scale as  $M_S$ ; hence  $D$ -strain produces a linear width ( $\Delta\text{energy}$ ) dependence on  $M_S$ , which projects onto a width in field ( $\Delta\mathbf{B}$ ) that also scales linearly with  $M_S$ . The rounding close to  $M_S = 0$  is due to a convolution of the intrinsic lifetime (spin-lattice) broadening and the  $M_S$  dependent ( $D$ -strain) contribution. The former is expected to produce a Lorentzian lineshape, thus accounting for the apparent crossover from Gaussian to Lorentzian EPR lines, as observed for the sharper transitions in Fig. 4. The slight narrowing of the EPR widths in Fig. 5 as a function of increasing frequency, and the weak asymmetry about  $M_S = -1/2$ , is due to the fact that higher frequency (higher  $M_S$ ) transitions are observed at higher magnetic fields, where the inter-SMM dipolar broadening is weaker (see discussion below). For  $\text{Fe}_8\text{Br}$ , no measurable  $g$ -strain is observed. A theoretical analysis of these trends may be found in ref. [37].

The temperature dependent contribution to the linewidths for  $\text{Fe}_8\text{Br}$  (Fig. 6) is dominated by random/fluctuating dipolar fields at each SMM site, due to the moments of the surrounding SMMs. At 116 GHz, the  $M_S = -10$  to  $-9$  transition occurs very close to zero field ( $\sim 0.1$  T). Under zero field cooling, the spin-up ( $M_S = -10$ ) and spin-down ( $M_S = +10$ ) states will be equally populated. Hence, the random distribution of spin-up and spin-down molecules results in a maximal contribution to the Gaussian dipolar EPR line broadening, as evidenced by the extremely large temperature dependent contribution to the  $M_S = -10$  to  $-9$  transition in Fig. 6 as  $T \rightarrow 0$ . Upon raising the temperature, higher levels in the scheme ( $|M_S| < 10$ ) become populated and the individual moments begin to fluctuate more rapidly, thus leading to a suppression of the dipolar broadening. The same qualitative picture may be applied to the other transitions ( $M_S = -9$  to  $-9$  *etc.*), provided that  $k_B T$  exceeds the

Zeeman splitting of the ground state. For  $k_B T$  less than the ground state Zeeman splitting, the system polarizes and the dipole fluctuations are suppressed, leading to an EPR line narrowing, as confirmed for all but the  $M_S = -10$  to  $-9$  transition in Fig. 6. The crossover occurs when the  $M_S = +10$  state starts to depopulate, *i.e.* approximately when  $k_B T = gS\mu_B \mathbf{B}$ . The inset to Fig. 6 shows the crossover temperature ( $T_{CR}$ ), where the slope of the data in the main part of the figure changes sign, versus the average magnetic field strength at which each particular transition is observed (see Fig. 2). It is found that  $T_{CR}$  indeed scales linearly with  $\mathbf{B}$ . Furthermore, the slope of the fit to the data in the inset to Fig. 6 is  $14.4 \pm 1 \text{ K} \cdot \text{T}^{-1} = gS\mu_B/k_B$ , corresponding very well to  $S = 10$  and  $g \approx 2$  to within the experimental error, thus supporting the picture of dipolar broadening.

In Fig. 7, we show the temperature dependent shifts of the EPR line positions obtained from Fig. 2. When compared to Fig. 6, it is noticeable that there is a similar crossover in the temperature dependence for transitions from levels with  $|M_S| < 10$ . Therefore, this low-temperature limiting behavior may also be attributed to the polarization of the spin system. The sign of the shift indicates that the field at each SMM site, due to neighboring SMMs, opposes the applied field, *i.e.* it is opposite to the polarization direction. This is to be expected for the  $\text{Fe}_8\text{Br}$  structure, in which the  $\text{Fe}_8$  molecules reside on the corners of a slightly distorted cube [54]. From the magnitudes of the  $|M_S| < 10$  line shifts, we estimate dipolar fields at each SMM site of a few hundred Gauss ( $\sim 300 \text{ G}$ ). The origin of the continued shift of the  $M_S = -10$  to  $-9$  transition to lower magnetic fields is, at present, not well understood.

A comprehensive theoretical analysis of this linewidth data has been published elsewhere [37]. From such an analysis for the sample used in obtaining the data in Fig. 2, we estimate a distribution in  $D$  of  $\sigma_D = 0.01D$ , negligible  $g$ -strain, and a dipolar contribution to the broadening which assumes a nearest neighbor SMM separation of  $12 \text{ \AA}$  [55], which is in agreement with the accepted range of near neighbor distances of between  $10.5 - 14 \text{ \AA}$ . Within acceptable ranges, no other combination of parameter values is able to produce the same quality of fit simultaneously to all of the frequencies and temperatures studied for this

particular sample, even though other parameter values may produce good fits for a particular measurement. This emphasizes the power of our multi-frequency single crystal EPR technique.

Very recent studies on a different sample from the one used in the measurements described above (similar shape and size, and obtained from the same synthesis), reveal unusual line-shape characteristics, particularly at low temperatures and for transitions involving levels close to the bottom of the potential wells (*e.g.*  $M_S = -10 \rightarrow -9$  and  $M_S = -9 \rightarrow -8, \dots$ ). This is illustrated in Fig. 8, for data obtained at a frequency of 145.937 GHz, with the field aligned precisely along the easy axis. At the somewhat elevated temperature of 10 K (Fig. 8a), the  $M_S = -10 \rightarrow -9$  transition shows appreciable asymmetry: this resonance has a Lorentzian (dotted curve) tail on the low field side, and closer to a Gaussian (dashed curve) tail on the high field side; furthermore, the data lie somewhat to the right of the fits on the high field side. Subsequent resonances ( $M_S = -9 \rightarrow -8$ ,  $M_S = -8 \rightarrow -7$ , *etc.*) appear to be less asymmetric, and the Gaussian fit improves. Recent theoretical studies have considered, in some detail, the effects of different types of dislocation on EPR lineshapes, and how these dislocations may influence the MQT phenomenon in SMMs (see section V) [40,56]. Both Lorentzian and Gaussian broadening are predicted [40], as well as asymmetry [56] (see discussion in section V).

Examination of the  $M_S = -10 \rightarrow -9$  transition at lower temperatures (Fig. 8b) reveals a possible fine structure to the line, which is strongly temperature dependent. At present, it is unclear whether the observed fine structure and asymmetry is due to sample quality, or whether there is a physical explanation for these effects. A direct comparison with the data in Figs. 3 and 4 is complicated by the fact that the linewidths are substantially broader for this second sample (increased  $D$ –strain); we note that many SMM compounds are known to lose solvent molecules [57], which could lead to a degradation of sample quality over time and may, in fact, provide a natural explanation for the  $D$ –strain. Nevertheless, the  $M_S = -10 \rightarrow -9$  transition in Fig. 2 (lowest field resonance) also exhibits fine structure at the lowest temperatures, and fine structure is also apparent in data published by Barra *et al.* [33]. It is

conceivable that the fine structure is indicative of a finite number of SMM site symmetries, as opposed to a smooth distribution. The dislocation theory of Garanin and Chudnovsky [40] leads to long range strains in the crystal, thus giving rise to a smooth distribution in site symmetries. Therefore, the fine structure we observe may signify a finite number of configurations involving  $\text{Fe}_8$  molecules coordinated by different numbers or arrangements of ligand molecules. It should be stressed that the data presented in Fig. 8 truly represent the intrinsic EPR lineshapes, *i.e.* any instrumental effects would be systematic and, therefore, influence all of the lineshapes equivalently. Clearly, additional studies on a range of samples prepared in different ways, *i.e.* different sample qualities, will be required to fully resolve these issues – such studies are currently in progress.

Finally, a possible clue as to the origin of the anomalous temperature dependence of the  $M_S = -10 \rightarrow -9$  EPR transition linewidth, as seen in Fig. 6, comes from the fact that the magnitude of the microwave absorption becomes temperature independent below about 6 K (see 2.1 K and 4.5 K traces in Fig. 8 b). This could indicate that this particular transition saturates at the lowest temperatures, due to the diverging spin-lattice relaxation time. Unfortunately, the microwave power at the location of the sample is not well known in our set up, thus precluding an estimate of  $T_1$ .

## B. $\text{Mn}_{12}-\text{ac}$

Figure 9 shows raw data obtained for  $\text{Mn}_{12}-\text{ac}$  at a frequency of 189.123 GHz, and at temperatures between 10K and 35K; the field is applied parallel to the easy axis to within  $0.2^\circ$ . The first point to note is the diminished signal-to-noise for this data, when compared to Fig. 2. There are several reasons for this: first, the dynamic range of our spectrometer is reduced at this higher frequency of 189 GHz; second, the volume of the sample used in this investigation was somewhat smaller than that of the  $\text{Fe}_8\text{Br}$  sample used for the studies in the previous section; finally, due to the increased energy scale of the  $\text{Mn}_{12}-\text{ac}$  system (larger  $|D|$ ), the observed transitions correspond to levels considerably higher in energy above the ground state than would be the case for  $\text{Fe}_8\text{Br}$  at comparable frequencies and

fields. Therefore, this constitutes a much more challenging experiment. Nevertheless, clear resonances are observed, which also have Gaussian lineshapes (solid curves), and once again exhibit a pronounced linewidth dependence on  $M_S$  (the level from which the transition was excited). For comparison, the inset to Fig. 9 shows attempts to fit the first two transitions with Gaussian and Lorentzian functions; the Gaussian fit is noticeably better.

Figure 10 plots the  $M_S$  dependence of the Gaussian EPR linewidths for measurements made at several different frequencies. The linear  $M_S$  contribution to the widths once again indicates a significant distribution in  $D$  ( $\sigma_D \sim 0.02D$ ). However, the dipolar contribution to the linewidths is considerably weaker for  $Mn_{12}-ac$  than for  $Fe_8Br$ . This is initially apparent from the weak frequency dependence observed amongst the widths for transitions with  $|M_S| < 5$ , and the fact that the frequency dependence observed for higher  $|M_S|$  transitions is opposite to what was observed for  $Fe_8$  in Fig. 5, *i.e.* the higher frequency transitions are broader. The origin of this effect has to do with  $g$ -strain, and will be discussed further below.

In Fig. 11, we plot the temperature dependence of the linewidths observed at a frequency of 189.123 GHz. A similar trend can be observed for the low  $|M_S|$  transitions for both  $Mn_{12}-ac$  and  $Fe_8Br$  (decreasing width with decreasing temperature). However, the pronounced line narrowing observed for the higher  $|M_S|$  transitions at lower temperatures, in  $Fe_8Br$ , is absent in  $Mn_{12}-ac$ . This provides further evidence that the dipolar contribution to the linewidths is considerably weaker in  $Mn_{12}-ac$ . In contrast, the  $M_S$  dependence of the widths is stronger for  $Mn_{12}-ac$ , due to the increased  $D$ -strain ( $\sigma_D \approx 0.02D$ , as opposed to  $\sigma_D \approx 0.01D$  for  $Fe_8Br$ ). The weaker dipolar broadening is consistent with an increased inter-SMM separation for  $Mn_{12}-ac$  [2].

The pronounced frequency dependence of the larger  $|M_S| (> 5)$  transitions, as seen in Fig. 10, is attributable to  $g$ -strain. Each transition shifts to higher field with increasing frequency, thereby amplifying the effect of a distribution in  $g$  – hence the increased linewidths with increasing frequency. Additional support for  $g$ -strain comes from the measured anisotropy in the  $g$ -tensor, both from our previous work [26] and that of others [31,32].

Using accepted values for the inter-SMM separations, it is possible to simulate all data obtained for a particular sample with a single pair of (sample dependent)  $D$ – and  $g$ –strain parameters;  $\sigma_D = 0.02D$  and  $\sigma_g = 0.008g$  are typical for many of the  $\text{Mn}_{12}\text{--ac}$  samples we have studied [37].

Finally, in Fig. 12, we show magnifications of several of the resonances from Fig. 9. Once again, it is apparent that the EPR lines exhibit a fine structure. In particular, the  $M_S = -6$  to  $-5$  and  $M_S = -5$  to  $-4$  transitions show a clear double peak structure; the best attempts at single Gaussian fits (dotted curves) are included in the figure for comparison. Similar behavior was observed at other frequencies. Once again, these findings hint at the possibility that there may exist a finite number of configurations involving  $\text{Mn}_{12}\text{--ac}$  molecules coordinated by different numbers or arrangements of ligand molecules. We note that the presence of various isomeric forms of  $\text{Mn}_{12}$ , whereby the arrangements of the ligands differ slightly, is well established both in the acetate [58] and in  $\text{Mn}_{12}$  SMMs involving other ligands [59].

## V. Discussion

The unambiguous demonstration of  $D$ –strain in  $\text{Fe}_8\text{Br}$  and  $\text{Mn}_{12}\text{--ac}$  indicates the presence of significant sample inhomogeneities or imperfections, *i.e.* the molecules are subjected to varying anisotropy. A natural explanation for this could be a loss of solvent molecules, or disorder among the ligands; indeed a slight degradation of sample quality over time has been noted, and it is known that the crystals do lose solvent [57]. Another possibility has recently been proposed by Garanin and Chudnovsky [40], involving dislocations in the crystals which act to locally distort the site symmetries of individual SMMs. What is more, Garanin and Chudnovsky have claimed that the QTM phenomenon in SMMs finds a natural explanation in terms of these dislocations. As mentioned in the introduction, QTM requires symmetry breaking terms in the Hamiltonian (Eq. 1). Local rotations of the magnetic anisotropy axes due to dislocations have two effects: they generate transverse second order crystal field terms, of the form  $E(\hat{S}_x^2 - \hat{S}_y^2)$ , which facilitate QTM between  $M_S$  states differing by an even integer;

and they result in an effective local transverse magnetic field (under application of field  $\parallel z$ ) that unfreezes odd tunneling resonances, thereby solving the conundrum as to why both even and odd tunneling resonances are always observed in  $\text{Fe}_8\text{Br}$  and  $\text{Mn}_{12}-\text{ac}$ . It has also been shown that long-range strains produced by dislocations result in broad distributions of relaxation times, something which is also observed experimentally in  $\text{Mn}_{12}-\text{ac}$  [40]. Indeed, assuming realistic concentrations of dislocations, Garanin and Chudnovsky [40] have been able to account for the experimentally observed tunneling in  $\text{Mn}_{12}-\text{ac}$  [49], and predict a distribution in the uniaxial spin-spin coupling parameter  $\sigma_D \approx 0.027D$ , which is of the same order as we have found from linewidth analyses ( $\sigma_D \approx 0.01 - 0.02D$ ). It should be pointed out, however, that any disorder amongst the ligand molecules, as well as any loss of solvent molecules, may be expected to produce many of the same effects as those proposed by Garanin and Chudnovsky [40], *i.e.* disorder amongst the peripheral molecules surrounding the SMMs will result in local variations in site symmetry.

Careful theoretical consideration of different forms of dislocations (edge, screw, correlated, uncorrelated, *etc.*) indicate that the resultant  $D$ -strain can produce both Gaussian and Lorentzian EPR lineshapes [40]. Furthermore, recent work by Park *et al.* [56], predicts asymmetry in some of the EPR lineshapes; one may think of this as arising due to the fact that a dislocation causes an asymmetric distribution in  $D$ , *i.e.* it can only reduce  $D$ , not enhance it. Clearly, certain features of the results presented here, particularly in Fig. 8a, may confirm some of these predictions. So far, our attempts to simulate data have been limited to  $D$ -strain,  $g$ -strain and dipolar broadening. The  $D$ - and  $g$ -strains should be correlated, although we have yet to verify this. Simulated  $E$ -strain, as well as strain in the fourth order anisotropy, did not affect our simulations to within sensible ranges of these parameters. We have also ignored hyperfine effects, since these are irrelevant in the case of the  $\text{Fe}_8\text{Br}$  ( $^{56}\text{Fe}$  has no nuclear spin), and exchange narrowing in  $\text{Mn}_{12}-\text{ac}$  is believed to diminish the hyperfine splitting [37]. At present, most of our data have been obtained for just a few samples of each of  $\text{Fe}_8\text{Br}$  and  $\text{Mn}_{12}-\text{ac}$ . Further work is in progress on a range of different SMMs, with the goal of resolving some of these issues, *e.g.* whether solvent loss or

ligand disorder is the main reason for the observed  $D$ –strain, or whether EPR lineshapes correlate with various theoretical works in progress dealing with dislocation mediated QTM [56].

Clearly, if the QTM mechanism is mediated by disorder, then single crystal EPR offers the most direct means of providing quantitative information with which to test relevant theoretical predictions. However, it is essential that EPR lineshapes obtained from experiments are free from the experimental artifacts which have been known to plague high frequency EPR measurements. Indeed, given the strong  $M_S$  dependence of the EPR line shapes and widths, one has to question recent attempts to determine the crystal field parameters to fourth order from high frequency EPR. Inspection of the fits to data for  $\text{Fe}_8\text{Br}$  and  $\text{Mn}_{12}\text{--ac}$  by Barra *et al.* [8,32,33,34], reveal considerable discrepancies in the positions of low  $|M_S|$  transitions. Because of the smaller linewidths associated with the low  $|M_S|$  transitions, one can be far more confident as to the experimentally determined resonance field from such transitions, than one can be for the considerably broader high  $|M_S|$  resonances. Field modulation techniques compound this problem, as do studies on aligned polycrystals which give rise to asymmetric distributions in the orientations of the individual crystallites. Indeed, our most recent investigations indicate that the high frequency EPR technique described in this article (section III and [28,52]) yields crystal field parameters that are in much closer agreement with inelastic neutron scattering measurements than conventional high field EPR studies [60].

## VI. Summary and conclusions

We have used a multi-high frequency cavity perturbation technique to measure EPR lineshapes for oriented single crystal samples of the  $\text{Fe}_8\text{Br}$  and  $\text{Mn}_{12}\text{--ac}$  SMMs. The use of a narrow band cavity offers many important advantages over non-resonant methods: careful consideration concerning the coupling of radiation to and from the cavity (via waveguide), combined with the ability to study very small samples, eliminates mixing of the dissipative and reactive responses of the sample under investigation, and enables faithful extraction of

the true EPR lineshapes. Our ability to measure at many frequencies, temperatures and orientations further allows us to distinguish between several contributions to the EPR line widths and shapes. These include: inter-SMM and hyperfine dipolar fields; distributions in crystal field parameters; and spin-lattice interactions. Each of these effects have been discussed in the literature in terms playing a possible role in the MQT phenomenon. In addition to significant  $D$ –strain, which is indicative of a distribution in the SMM site symmetries, we have detected a previously unobserved fine structure to some of the resonances for both  $\text{Fe}_8\text{Br}$  and  $\text{Mn}_{12}\text{--ac}$  SMMs.

## VII. Acknowledgements

We would like to thank George Christou, David Hendrickson and Andrew Kent for useful discussion. This work was supported by the National Science Foundation (DMR0103290 and DMR0196430). S. H. is a Cottrell Scholar of the Research Corporation.

---

## VIII. References cited

† email: hill@phys.ufl.edu

- [1] D. Gatteschi, A. Caneschi, L. Pardi, and R. Sessoli, *Science* **265**, 1054 (1994).
- [2] T. Lis, *Acta Crystallogr.* **B36**, 2042 (1980).
- [3] R. Sessoli, H. Tsai, R. Schake, S. Wang, J. B. Vincent, K. Folting, D. Gatteschi, G. Christou, D. N. Hendrickson, *J. Am. Chem. Soc.* **115**, 1804 (1993).
- [4] R. Sessoli, D. Gatteschi, A. Caneschi, and M. A. Novak, *Nature* **365**, 141 (1993).
- [5] B. Schwarzschild, *Physics Today* **50**, 17 (1997).
- [6] P.E.C. Stamp, *Nature* **383**, 125 (1996).

[7] K. Wieghart, K. Pohl, I. Jibril, G. Huttner, *Angew. Chem. Int. Ed. Engl.* **23**, 77 (1984).

[8] A-L. Barra, P. Debrunner, D. Gatteschi, Ch.E. Schulz, R. Sessoli, *Europhys. Lett.* **35**, 133 (1996).

[9] D. Gatteschi, A. Caneschi, R. Sessoli, and A. Cornia, *Chem. Soc. Rev.* 101 (1996).

[10] J. Kortus and M. R. Pederson, *Phys. Rev. B* **62**, 5755 (2000).

[11] E. M. Chudnovsky, J. Tejada, *Macroscopic Quantum Tunneling of the Magnetic Moment*, Cambridge University Press, Cambridge, 1998.

[12] C. Paulsen, J-G. Park, B. Barbara, R. Sessoli, and A. Caneschi, *J. Magn. Magn. Mater.* **140-144**, 379 (1995).

[13] P. Politi, F. Rittori, F. Hartmann-Boutron, J. Villain, *Phys. Rev. Lett.* **75**, 537 (1995).

[14] J.R. Friedman, M.P. Sarachik, J. Tejada, R. Ziolo, *Phys. Rev. Lett.* **76**, 3830 (1996).

[15] L. Thomas, F. Lioni, R. Ballou, D. Gatteschi, R. Sessoli, B. Barbara, *Nature (London)* **383**, 145 (1996).

[16] J.A.A.J. Perenboom, J.S. Brooks, S. Hill, T. Hathaway, N.S. Dalal, *Phys. Rev. B* **58**, 330 (1998).

[17] C. Sangregorio, T. Ohm, C. Paulsen, R. Sessoli, D. Gatteschi, *Phys. Rev. Lett.* **78**, 4645 (1997).

[18] W. Wernsdorfer, A. Caneschi, R. Sessoli, D. Gatteschi, A. Cornia, V. Villar, C. Paulsen, *Phys. Rev. Lett.* **84**, 2965 (2000).

[19] F. Luis, J. Bartolome, J.F. Fernandez, J. Tejada, J.M. Hernandez, X.X. Zhang, R. Ziolo, *Phys. Rev. B* **55**, 11448 (1997).

[20] F. Fominaya, J. Villain, P. Gandit, J. Chaussy, and A. Caneschi, *Phys. Rev. Lett.* **79**, 1126 (1997).

[21] M. Hennion, L. Pardi, I. Mirebeau, E. Suard, R. Sessoli, A. Caneschi, *Phys. Rev. B* **56**, 8819 (1997).

[22] I. Mirebeau, M. Hennion, H. Casalta, H. Andres, H. U. Gudel, A. V. Irodova, and A. Caneschi, Phys. Rev. Lett. **83**, 628 (1999).

[23] R. Caciuffo, G. Amoretti, A. Murani, R. Sessoli, A. Caneschi, D. Gatteschi, Phys. Rev. Lett. **81**, 4744 (1998).

[24] A. Lascialfari, Z.H. Jang, F. Borsa, P. Carretta, D. Gatteschi, Phys. Rev. Lett. **81**, 3773 (1998).

[25] Z. H. Jang, A. Lascialfari, F. Borsa, and D. Gatteschi, Phys. Rev. Lett. **84**, 2977 (2000).

[26] S. Hill, J. A. A. J. Perenboom, N. S. Dalal, T. Hathaway, T. Stalcup and J. S. Brooks, Phys. Rev. Lett. **80**, 2453 (1998).

[27] J. A. A. J. Perenboom, M. R. Schaapman, S. O. Hill, J. S. Brooks and N. S. Dalal, in *Physical Phenomena in High Magnetic Fields - III*, eds Z. Fisk, L. P. Gor'kov and J. R. Schrieffer, p469 (World Scientific, Singapore 1999).

[28] S. Hill, N. S. Dalal and J. S. Brooks, Appl. Magn. Reson. **16**, 237 (1999).

[29] S. Maccagnano, R. Achey, E. Negusse, A. Lussier, M.M. Mola, S. Hill, and N.S. Dalal, Polyhedron **20**, 1441 (2001).

[30] The identical experimental setup as that used in ref. [26] has been used for single crystal EPR by E. del Barco, J. M. Hernandez, J. Tejada, N. Biskup, R. Achey, I. Rutel, N. Dalal and J. S. Brooks, Phys. Rev. B **62**, 3018 (2000).

[31] A. Caneschi, D. Gatteschi, R. Sessoli, A-L. Barra, L-C. Brunel, M. Guillot, J. Am. Chem. Soc. **113**, 5873 (1991).

[32] A-L. Barra, D. Gatteschi, and R. Sessoli, Phys. Rev. B **56**, 8192 (1997).

[33] A-L. Barra, D. Gatteschi, R. Sessoli, Chem-Eur. J. **6**, 1608 (2000); also cond-mat/00023869.

[34] A-L. Barra, F. Bencini, A. Caneschi, D. Gatteschi, C. Paulsen, C. Sangregorio, R. Sessoli, L. Sorace, cond-mat/0101216.

[35] A. A. Mukhin, V. D. Travkin, A. K. Zvezdin, S. P. Lebedev, A. Caneschi and D. Gatteschi, *Europhys. Lett.*, **44** (6), 778 (1998); A. Mukhin, B. Gorshunov, M. Dressel, C. Sangregorio and D. Gatteschi, *Phys. Rev. B* **63**, 214411 (2001).

[36] Beth Parks, Joseph Loomis, Evan Rumberger, David Hendrickson and George Christou, *Pjphys. Rev. B* **64**, 184426 (2001).

[37] Kyungwha Park, M. A. Novotny, N. S. Dalal, S. Hill and P. A. Rikvold, submitted to *Phys. Rev. B*.

[38] R. Blinc, P. Cevc, D. Arčon, N. S. Dalal and R. M. Achey, *Phys. Rev. B* **63**, 212401 (2001).

[39] J. F. Fernández, F. Luis, and J. Bartolomé, *Phys. Rev. Lett.* **80**, 5659 (1998).

[40] E. M. Chudnovsky and D. A. Garanin, *Phys. Rev. Lett.* **87**, 187203 (2001); also cond-mat/0105195; also cond-mat/0105518; also D. A. Garanin and E. M. Chudnovsky, cond-mat/0107586.

[41] D. A. Garanin and E. M. Chudnovsky, *Phys. Rev. B* **56**, 11102 (1997).

[42] M. N. Leuenberger and D. Loss, *Phys. Rev. B* **61**, 1286 (2000).

[43] M. N. Leuenberger and D. Loss, *Phys. Rev. B* **61**, 12200 (2000).

[44] H. De Raedt, S. Miyashita, K. Saito, D. Garcia-Pablos and N. Garcia, *Phys. Rev. B* **56**, 11761 (1997).

[45] V. V. Dobrovitsky and A. K. Zvezdin, *Europhys. Lett.* **38** 377 (1997).

[46] N. V. Prokof'ev and P. C. E. Stamp, *Phys. Rev. Lett.* **80**, 5794 (1998).

[47] W. Wernsdorfer, T. Ohm, C. Sangregorio, R. Sessoli, D. Mailly, and C. Paulsen, *Phys. Rev. Lett.* **82**, 3903 (1999).

[48] W. Wernsdorfer and R. Sessoli, *Science* **284**, 133 (1999).

[49] J. R. Friedman, M. P. Sarachik, and R. Ziolo, *Phys. Rev. B* **58**, 14729 (1998).

[50] J. M. Hernandez, X. X. Zhang, F. Luis, J. Bartolome, J. Tejada and R. Ziolo, *Europhys. Lett.* **35**, 301 (1996).

[51] W. Bao, R. A. Robinson, J. R. Friedman, H. Casalta, E. Rumberger, and D. N. Hendrickson, [cond-mat/0008042](https://arxiv.org/abs/cond-mat/0008042).

[52] Monty Mola, Stephen Hill, Philippe Goy and Michel Gross, *Rev. Sci. Inst.* **71**, 186 (2000).

[53] This frequency coverage will soon be extended to  $> 600$  GHz.

[54] X. Martinez-Hidalgo, E. M. Chudnovsky and A. Aharony, *Europhys. Lett.* **55** (2), 273 (2001).

[55] The dipolar calculation makes the rather bold simplification of assuming the SMMs to be distributed on a simple cubic lattice.

[56] K. Park, M. A. Novotny, N. S. Dalal, S. Hill, P. A. Rikvold, accepted for publication in *J. Appl. Phys.* (2001); also [cond-mat/0111589](https://arxiv.org/abs/cond-mat/0111589).

[57] G. Christou, private communication.

[58] W. Wernsdorfer, R. Sessoli, D. Gatteschi, *Europhys. Lett.* **47**, 254 (1999).

[59] D. Ruiz, Z. Sun, S. M. J. Aubin, E. Rumberger, C. Incarvito, K. Folting, G. Christou, D. N. Hendrickson, *Mol. Cryst. Liq.* **335**, 413 (1999).

[60] S. Hill *et al.*, in preparation.

## Figure captions

Fig. 1 a) Schematic of the double potential well for a spin  $S = 10$  system in zero applied magnetic field, with a dominant easy axis crystalline anisotropy  $D\hat{S}_z^2$ , with  $D < 0$ ; the  $M_S = \pm 10$  "spin-up" and "spin-down" states lie lowest in energy. Pure QTM, directly between the unperturbed  $M_S = \pm 10$  states (as indicated), is possible if there exist terms in the Hamiltonian (Eq. 1) which mix these two levels. In the absence of pure QTM, a thermally assisted form of QTM may occur if states higher up in the scheme are mixed. b) Application of a magnetic field biases the wells, favoring population of the  $-M_S$  states. Whenever levels in the two wells come into resonance, direct QTM is possible, and accelerated relaxation occurs between the spin-up and the spin-down states, *i.e.* the relaxation may be considerably faster than the classical thermally activated relaxation over the top of the barrier. Resonant QTM has been observed in the form of sharp steps in the hysteresis loops of SMMs [16].

Fig. 2. Temperature (indicated in the figure) dependent microwave absorption amplitude for  $\text{Fe}_8\text{Br}$ , as a function of magnetic field, for measurements at 116.931 GHz; the field is applied parallel to the easy axis to within an accuracy of  $1^\circ$ . Sharp resonances are observed, which correspond to EPR transitions between the  $2S + 1$  spin states of the system – these are labelled in the figure.

Fig. 3. A close up of several  $\text{Fe}_8\text{Br}$  resonances obtained at 10 K and a frequency of 89.035 GHz, with the field applied approximately parallel to the easy axis; the levels involved in the transitions are indicated in the figure. The solid and dashed curves represent respective Gaussian and Lorentzian fits to the data.

Fig. 4. Further Gaussian and Lorentzian fits to  $\text{Fe}_8\text{Br}$  data (same experimental conditions as Fig. 3), illustrating the  $M_S$  (level from which the transition was excited – indicated in the figure) dependence of the widths. The horizontal scale has been offset and normalized to the widths of each resonance – the actual widths are indicated in the figure.

Fig. 5. A compilation of the  $M_S$  (level from which the transition was excited) dependence

of the Gaussian EPR linewidths obtained for  $\text{Fe}_8\text{Br}$  at 10 K and many different frequencies (indicated in the figure); see text for a discussion of the data.

Fig. 6. Temperature dependence of the Gaussian EPR linewidths obtained for different spin transitions (indicated in the figure); the data were obtained at a frequency of 116.931 GHz, with the field applied parallel to the easy axis. The inset plots the field dependence of the crossover temperature ( $T_{CR}$ ) – the temperature at which the linewidths reach a maximum – for the  $M_S = -9$  to  $-8$ ,  $-8$  to  $-7$ ,  $-7$  to  $-6$  and  $-6$  to  $-5$  transitions.

Fig. 7. Temperature dependence of the EPR line positions obtained for different spin transitions (indicated in the figure); the data were obtained at a frequency of 116.931 GHz, with the field applied parallel to the easy axis. The line shifts [ $\mu_o\text{H}(T)$ ] are plotted relative to the respective line positions at 50 K [ $\mu_o\text{H}(50 \text{ K})$ ].

Fig. 8a) A close up of several  $\text{Fe}_8\text{Br}$  resonances obtained at 10 K and a frequency of 145.937 GHz, with the field applied exactly parallel to the easy axis; the levels involved in the transitions are indicated in the figure. The solid and dashed curves represent respective Gaussian and Lorentzian fits to the data. b) Temperature dependence of the  $M_S = -10$  to  $-9$  transition in (a) illustrating the apparent fine structure to this line.

Fig. 9. Temperature (indicated in the figure) dependent microwave absorption amplitude for  $\text{Mn}_{12}-\text{ac}$ , as a function of magnetic field, for measurements at 189.123 GHz; the field is applied parallel to the easy axis. Sharp resonances are observed, which correspond to EPR transitions between the  $2S + 1$  spin states (indicated in the figure) of the system. The solid curves are Gaussian fits to the data; the inset shows attempts to fit both Gaussian (solid curve) and Lorentzian (dashed curve) functions to some of the data in the main part of the figure.

Fig. 10. A compilation of the  $M_S$  (level from which the transition was excited) dependence of the Gaussian EPR linewidths obtained for  $\text{Mn}_{12}-\text{ac}$  at 20 K and several different frequencies (indicated in the figure); see text for a discussion of the data.

Fig. 11. Temperature dependence of the Gaussian EPR linewidths obtained for several spin transitions (indicated in the figure) in  $\text{Mn}_{12}-\text{ac}$ ; the data were obtained at a frequency of 189.123 GHz, with the field applied parallel to the easy axis. For comparison, see data for  $\text{Fe}_8\text{Br}$  in Fig. 6.

Fig. 12. Magnifications of several of the 189.123 GHz traces shown in Fig. 9 (transitions and temperatures are indicated in the figure), illustrating an apparent fine structure.

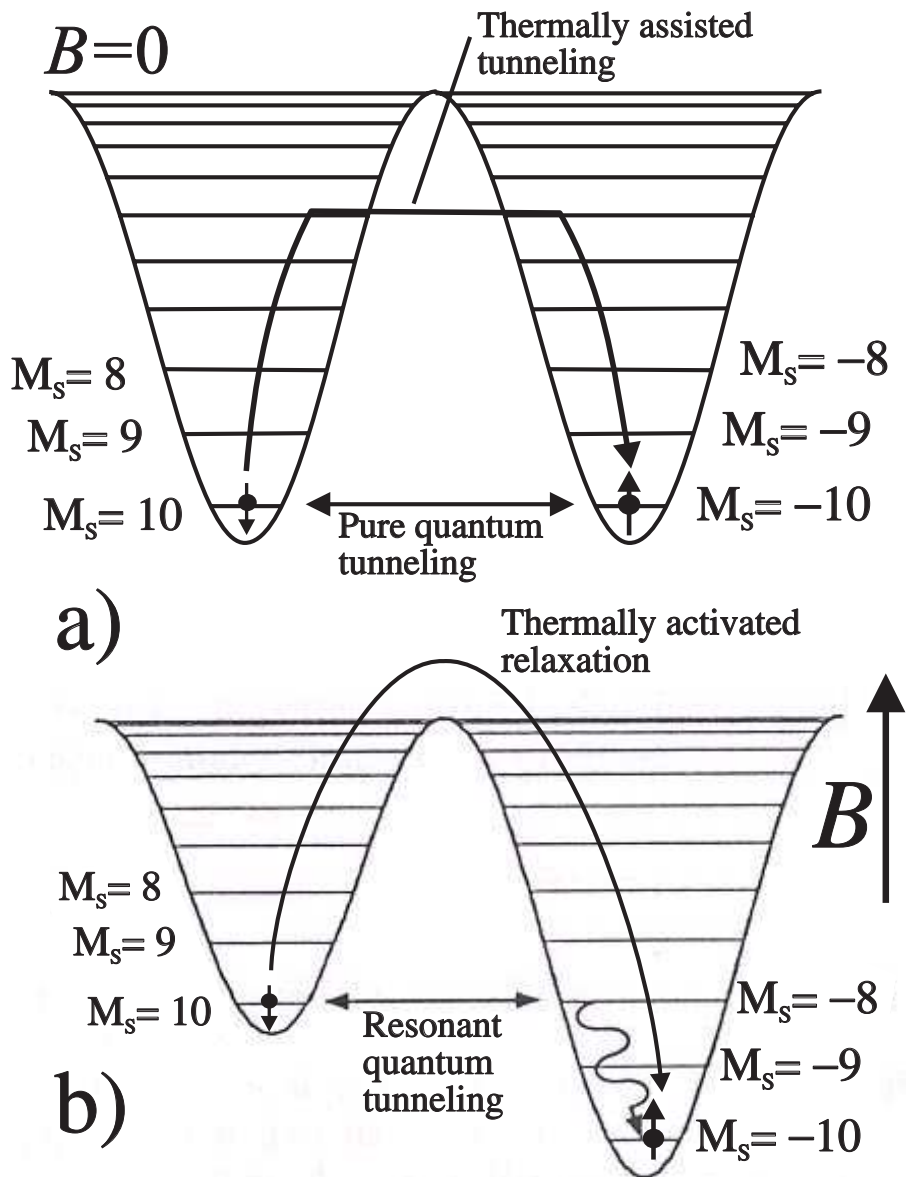


FIG. 1. Hill *et al.*

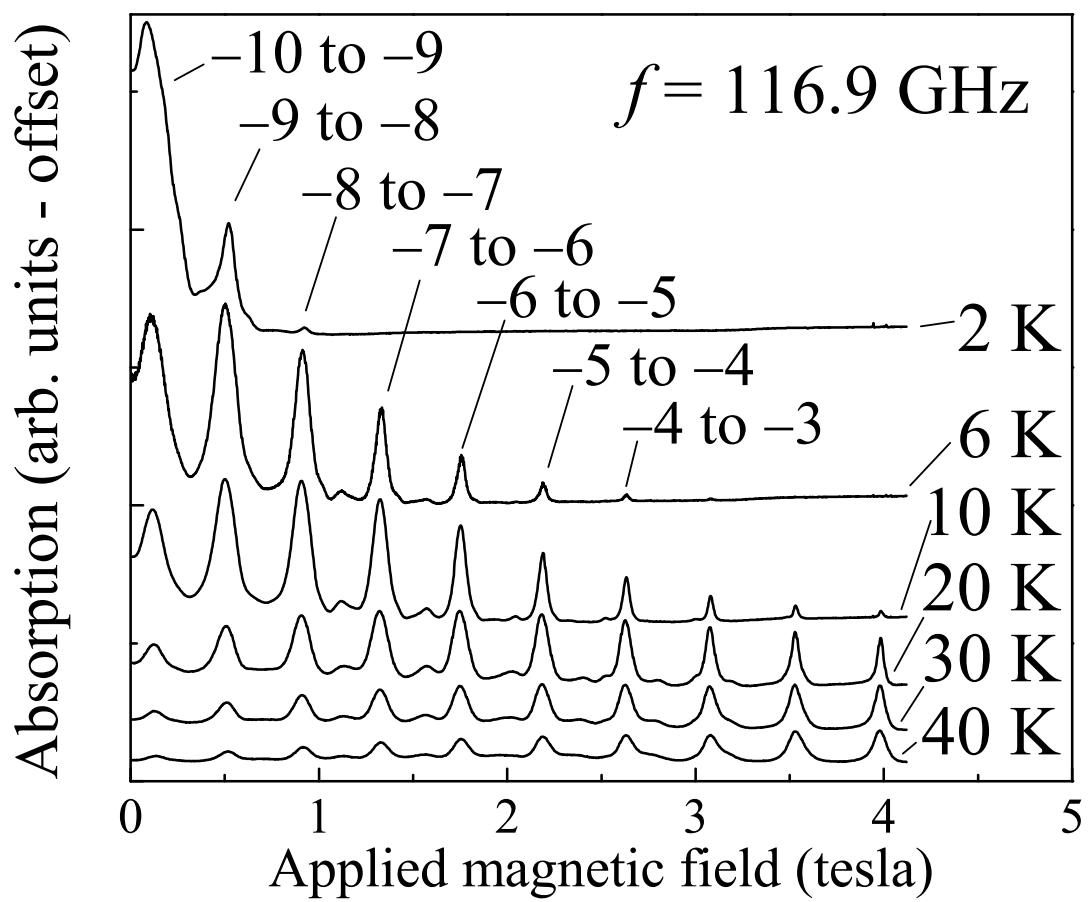


FIG. 2. Hill *et al.*

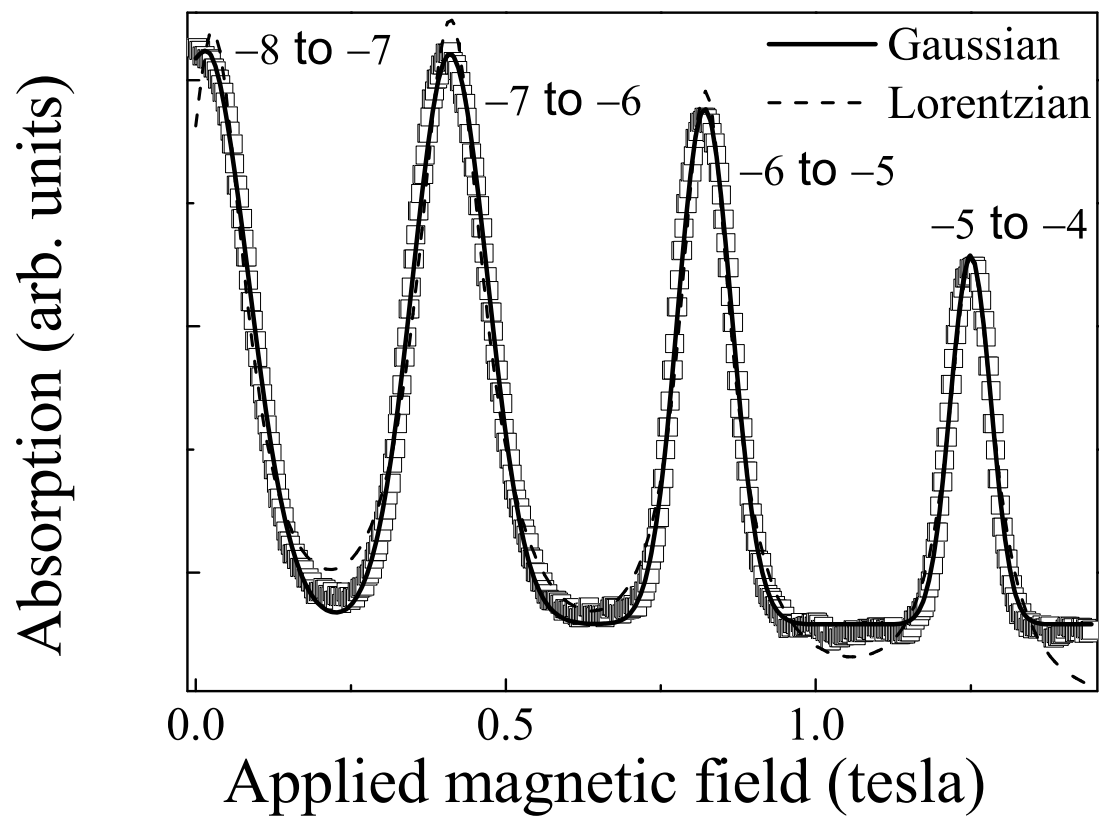


FIG. 3. Hill *et al.*

Absorption (arb. units)

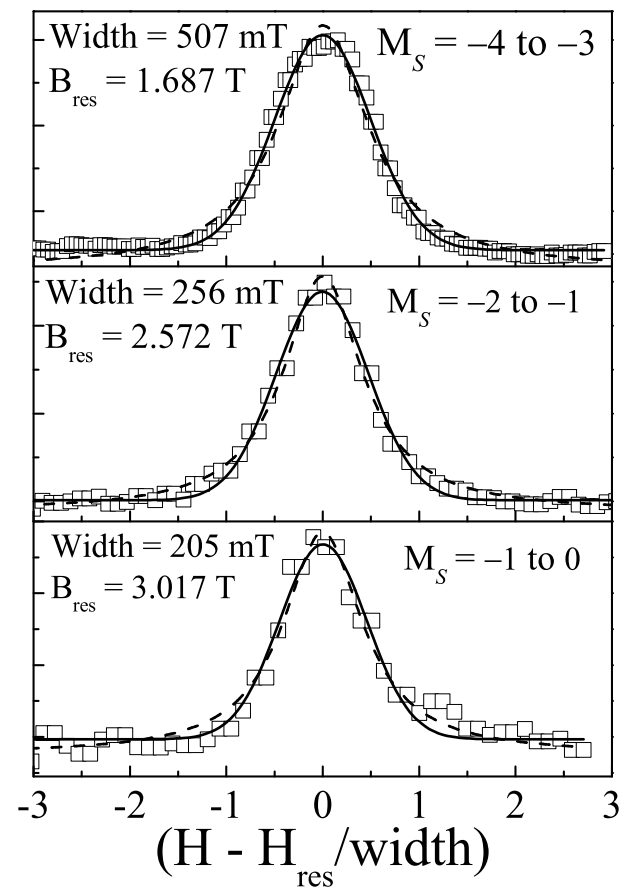


FIG. 4. Hill *et al.*

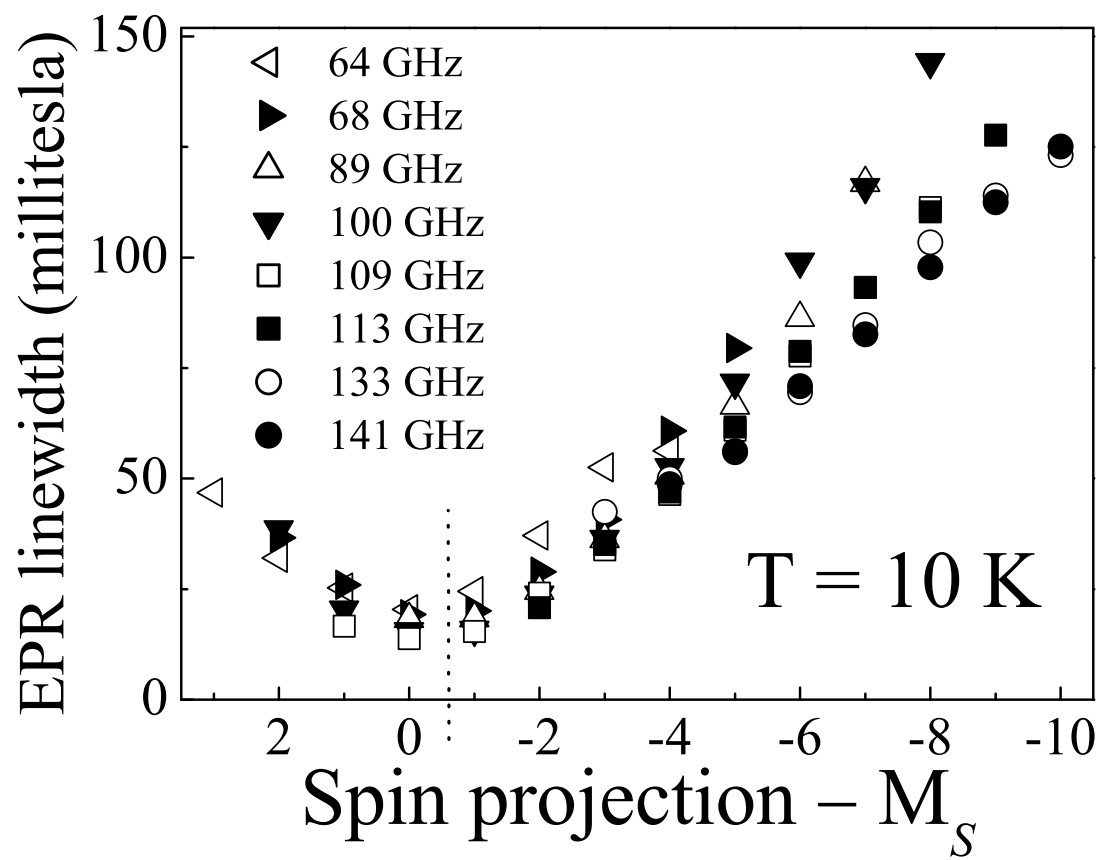


FIG. 5. Hill *et al.*

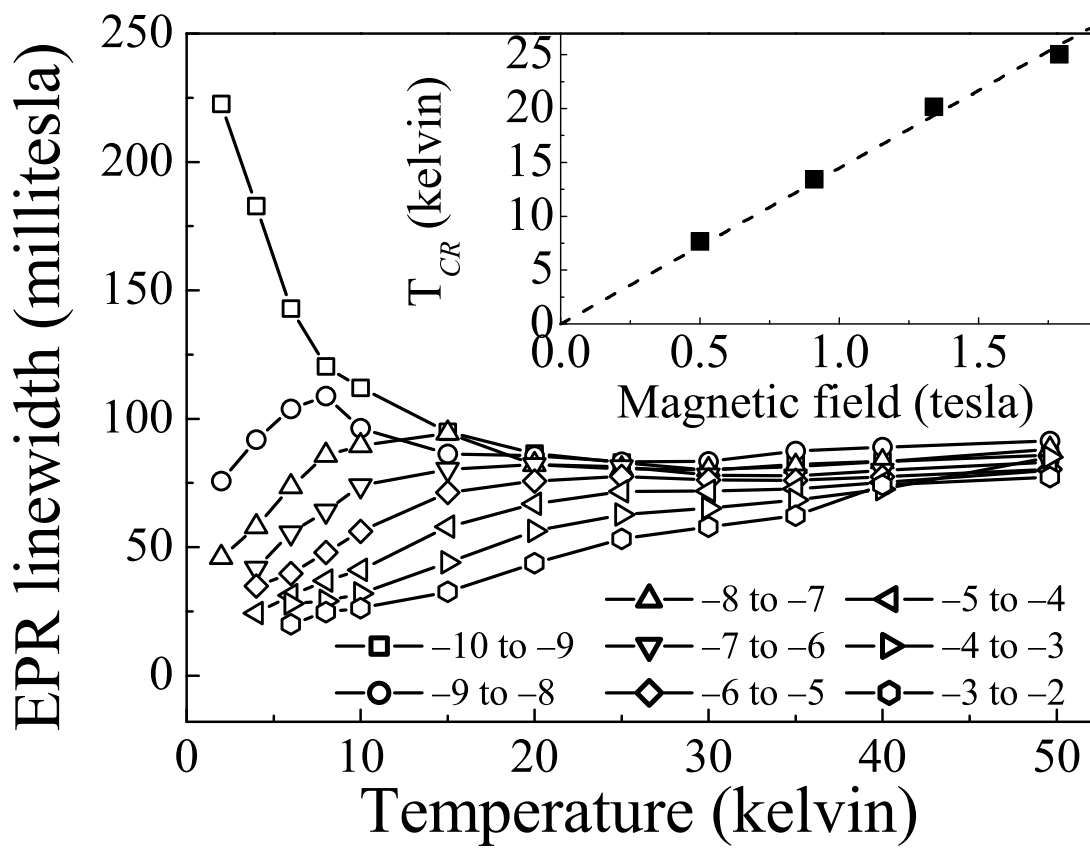


FIG. 6. Hill *et al.*

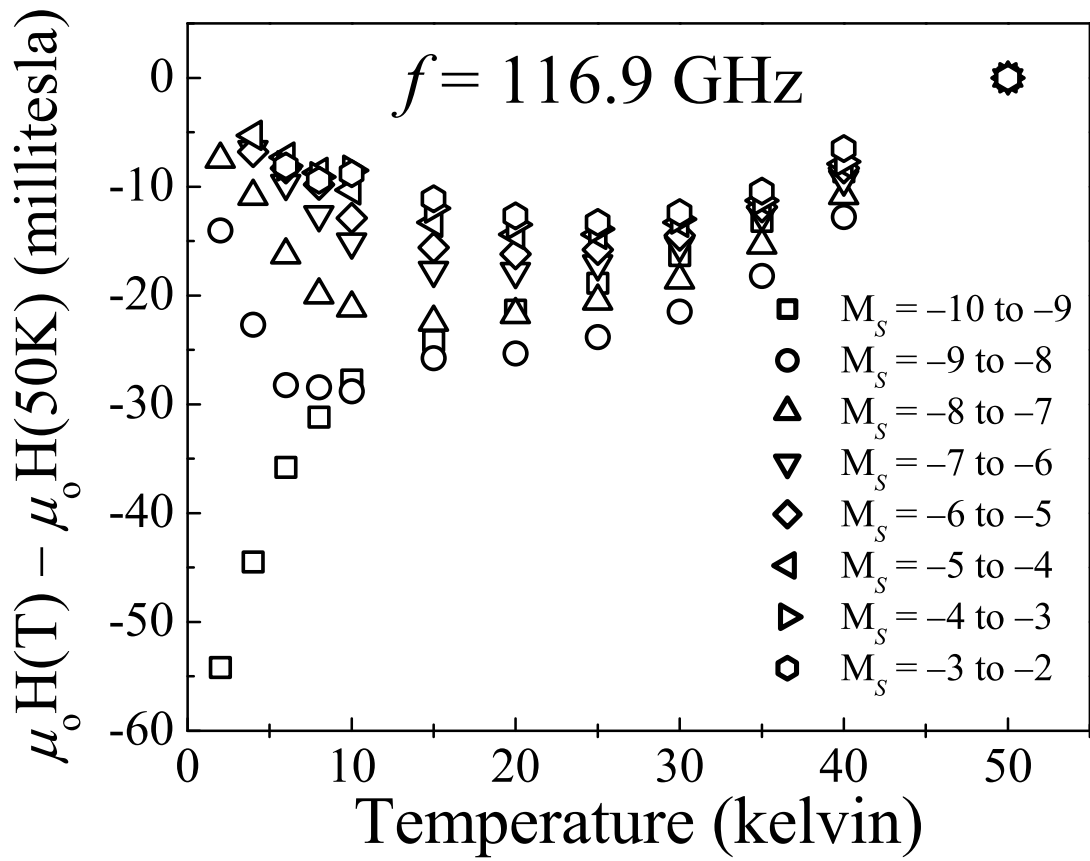


FIG. 7. Hill *et al.*

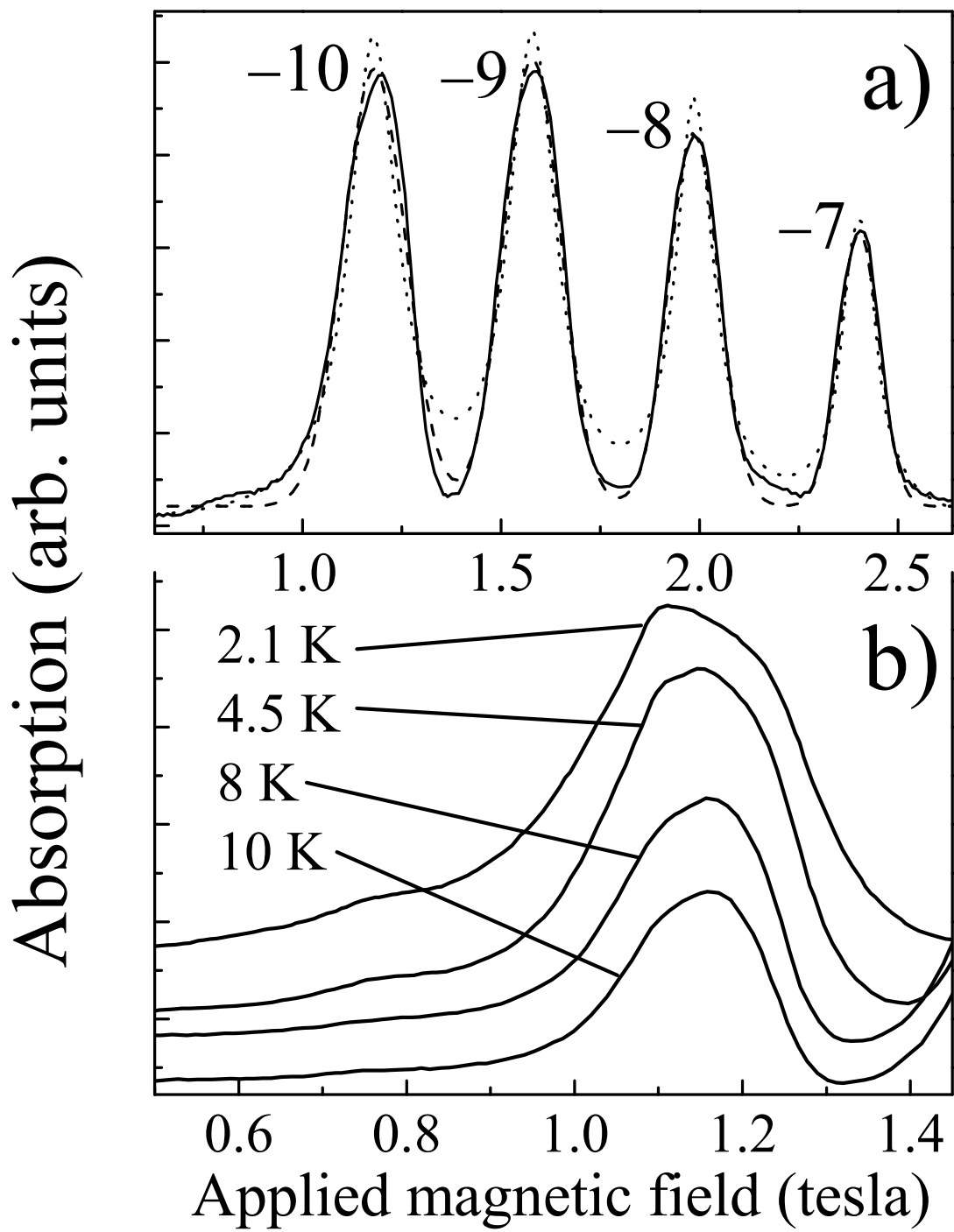


FIG. 8. Hill *et al.*

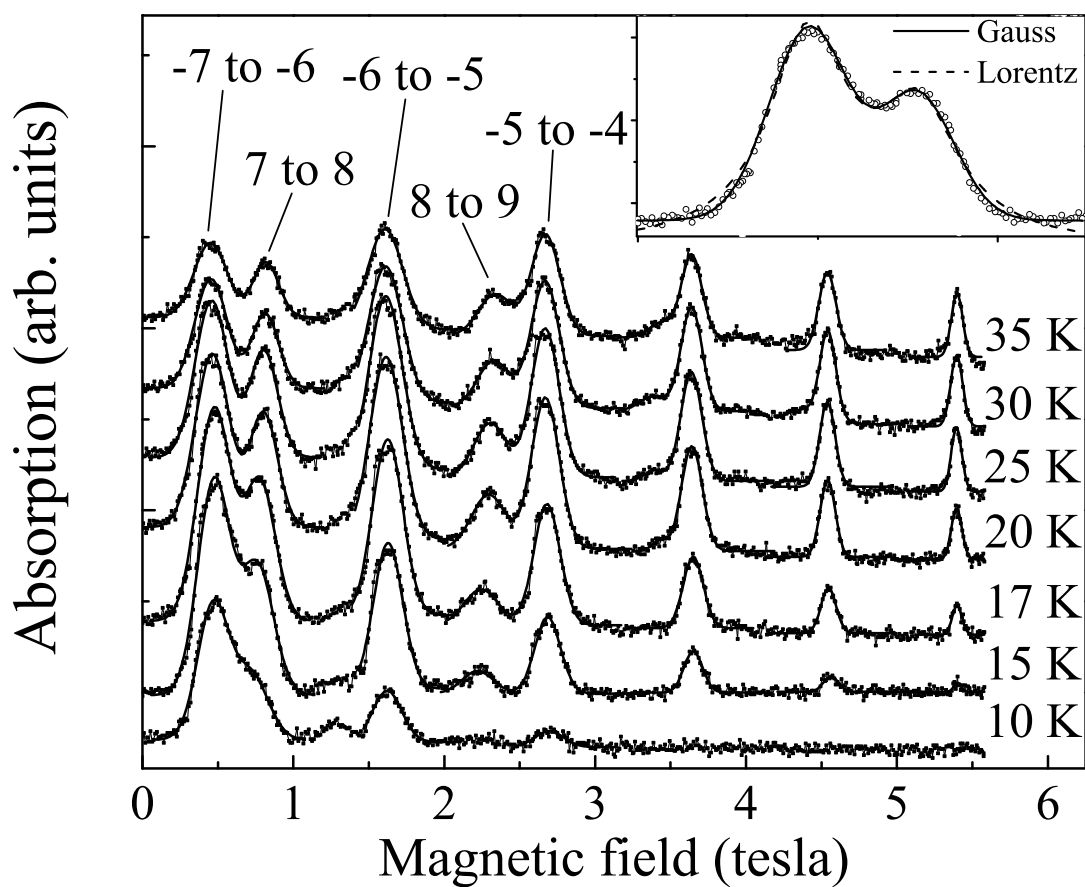


FIG. 9. Hill *et al.*

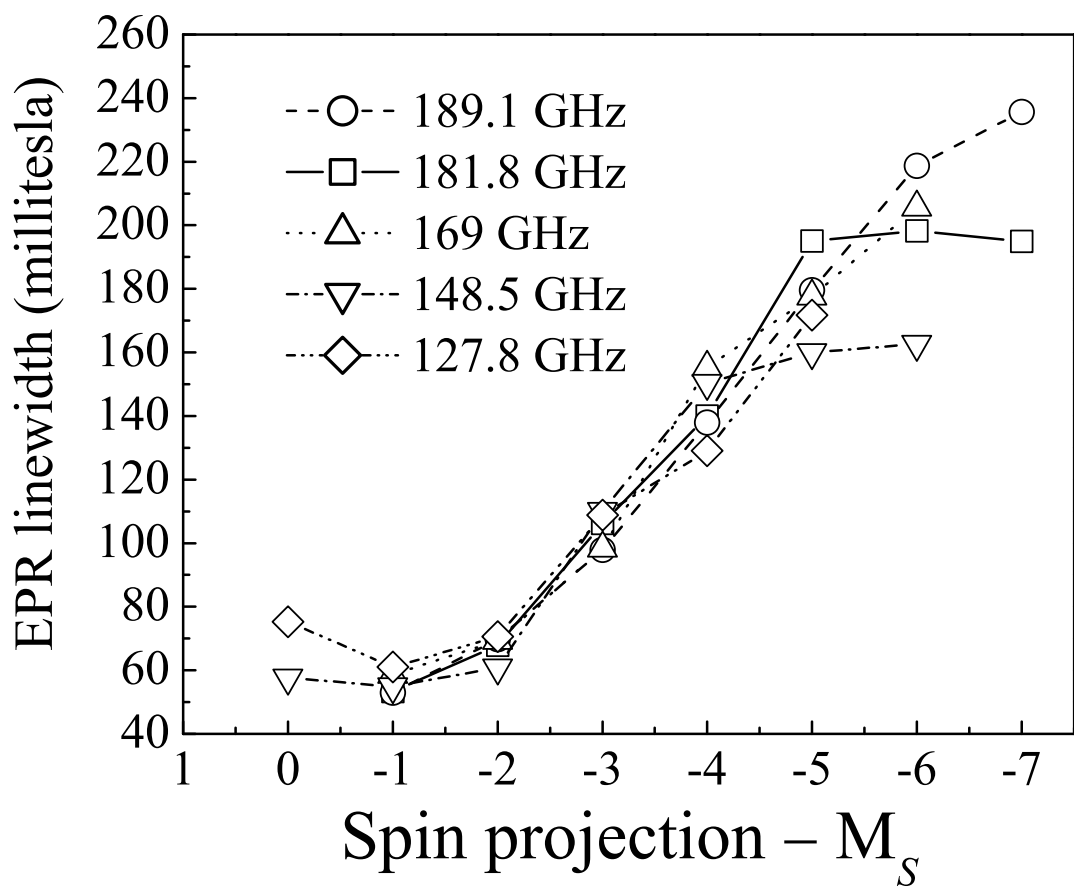


FIG. 10. Hill *et al.*

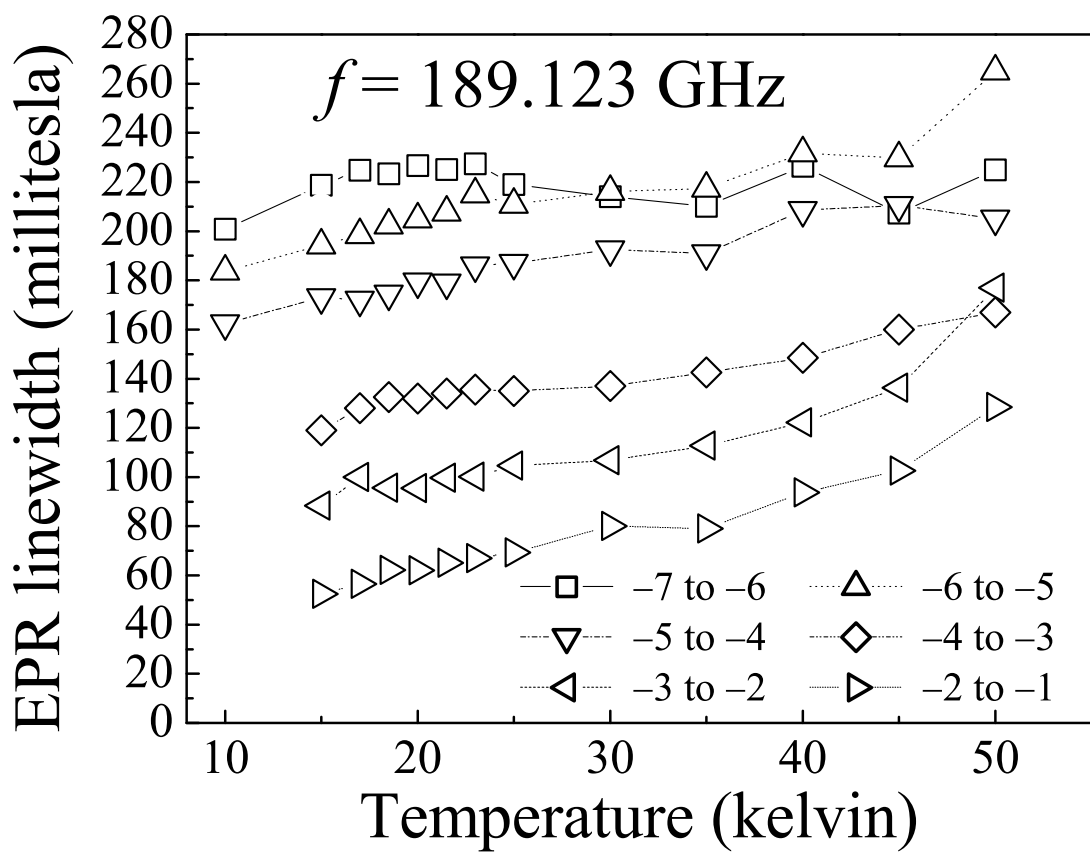


FIG. 11. Hill *et al.*

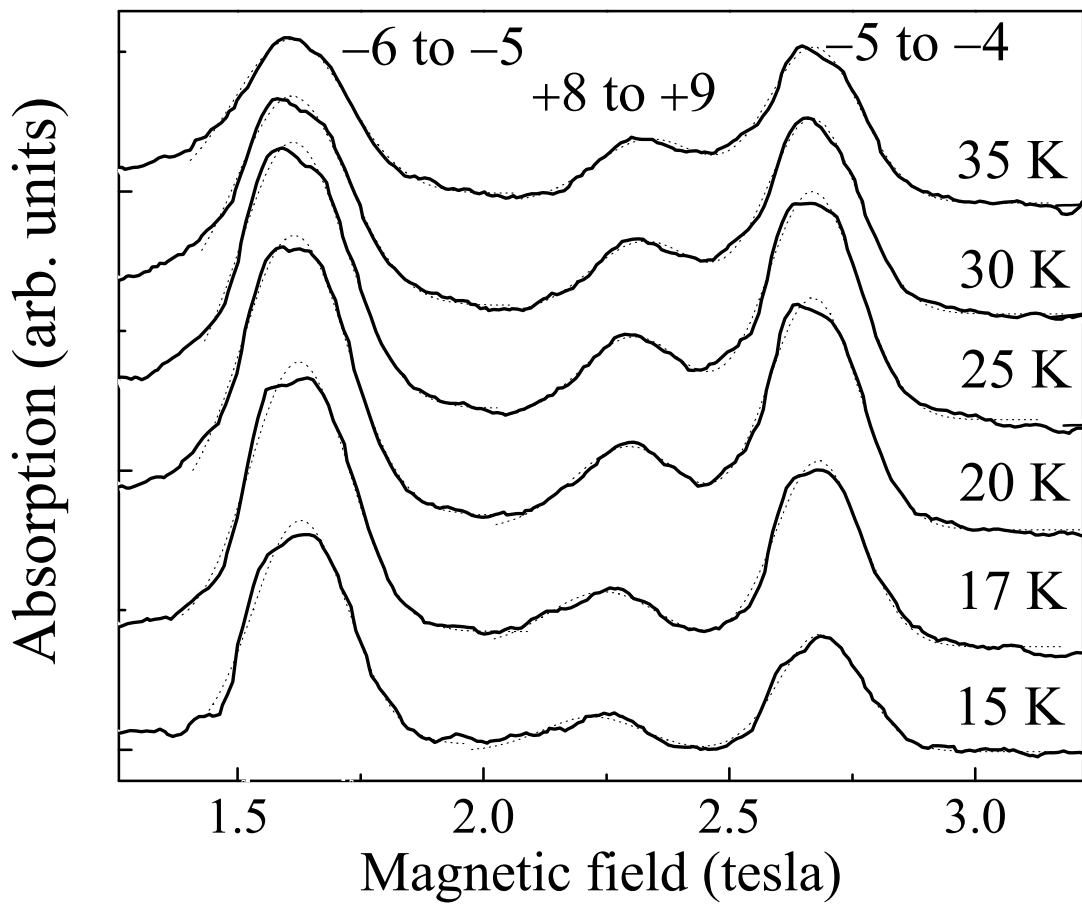


FIG. 12. Hill *et al.*